18. ACOUSTIC ANISOTROPY AND MICROFABRIC DEVELOPMENT IN ACCRETED SEDIMENT FROM THE NANKAI TROUGH[1]

W. Brückmann,[2] K. Moran,[3] and E. Taylor[4]

ABSTRACT

Complete penetration of frontal thrust and décollement of the Nankai Trough accretionary complex in Site 808 during ODP Leg 131 provided a wealth of structural observations and physical property data. In this paper possible mechanisms are discussed that could be responsible for the development of irregular downhole trends in acoustic anisotropy observed in Site 808. After various steps of data reduction and screening, a paleomagnetic reorientation procedure is applied to a selected group of physical property data sets. This facilitates the integration of the observed changes in physical properties with the geotectonic framework at the deformation front of the Nankai Trough accretionary complex. The paleomagnetic database was employed in the reconstruction of directional properties of acoustic velocities of the Lower Shikoku Basin sedimentary sequence, which is divided by a sharply defined décollement into an accreting and a subducting portion.

P-wave velocity anisotropies derived from paleomagnetically oriented samples in the upper part of this 420-m-thick hemipelagic sequence show maximum values in the direction parallel and normal to the inferred vector of plate convergence (310°–315°). No preferred orientation of *P*-wave velocity anisotropy is found in the subducting part of the sequence.

The preferred direction of maximum anisotropy parallel to the convergence vector is also in accordance with the true direction of the observed macro- to mesoscale structural features in Site 808. Microfractures and microcracks forming as stress relief and tensile fractures in cores of semilithified sediment normal and perpendicular to the maximum horizontal stress are discussed as control mechanisms for the development of the observed anisotropy pattern.

INTRODUCTION

General

The downhole development of anisotropies of various physical properties in suites of sedimentary sequences has received a great deal of attention; namely, acoustic anisotropies have been investigated since the days of DSDP by a number of workers (e.g., Carlson and Christensen, 1977; Carlson et al., 1983; Fuji, 1981; Wetzel, 1986). The reason for this continuing interest is obvious: if the development of acoustic anisotropy in different types of sediment and depositional environments could be easily correlated with specific genetic processes or typical microfabrics, it would represent a very fast and effective analytical tool for these properties. The term anisotropy refers to the observed quantitative directional dependence of physical properties of sediments. It is well known that most physical property anisotropies result from modifications of the pore-to-particle orientation during deposition and subsequent burial. Although this general rule applies also for acoustic anisotropy, there are a number of well-known or suspected second-order mechanisms that modify this simple case. In the following sections all of these will briefly be reviewed and discussed with respect to trends observed at Site 808.

Acoustic Anisotropy

In marine sediments with predominantly horizontal bedding compressional (*P*-wave) velocities generally show a downhole increase that is stronger in the direction parallel to the bedding plane, than perpendicular to it. This so-called acoustic anisotropy, A_p, is commonly defined as the difference between velocities in horizontal and vertical direction expressed as a percentage of the mean velocity:

$$A_p \ [4\%] = 200 \times (V_{pt}-V_{pl})/(V_{pt}+V_{pl})$$

where V_{pl} is the *P*-wave velocity determined in the direction parallel ("longitudinal") to the core axis core, V_{pt} the *P*-wave velocity in the horizontal ("transverse") direction. The positive transverse acoustic anisotropy normally ranges—depending on lithology and burial history—from values close to 0% near the surface to more than 12% at depths of several hundred meters.

A primary acoustic anisotropy will be generated in the course of deposition in current-dominated environments (Nacci et al., 1974; O'Brien, 1980). Comparing compositionally similar argillaceous sediments of hemipelagic and turbiditic origin from the Mississippi Fan, Wetzel (1987) found clear differences in patterns of strain and acoustic anisotropy. Turbiditic sediments display a stronger anisotropy parallel to the bedding plane as well as normal to bedding than do hemipelagic sediments. This so-called depositional anisotropy is attributed to the preferred orientation of elongated or oblate grains during turbiditic deposition. Acoustic anisotropy was also described as an intrinsic sedimentary property induced or amplified by alternating thin layers of isotropic or anisotropic materials (Postma, 1955; Bachman, 1979; Carlson et al., 1983), although this phenomenon has not been quantitatively observed under natural conditions.

An important mechanism for the generation of acoustic anisotropy is the development of preferred orientation of calcite *c*-axis normal to bedding in carbonate-rich marine sediments (O'Brien, 1990). This results in acoustic anisotropy, as the compressional *P*-wave velocity, V_p, is lowest parallel to the *c*-axis of calcite crystals, and highest parallel to their *a*-axis. Diagenetic reprecipitation of dissolved calcite normal to bedding, due, for example, to deformation, is frequently cited as a possible mechanism to create a uniform orientation of calcite crystals (Carlson and Christensen, 1979; Milholland et al., 1980). Primary deposition of oriented fragments of biogenic calcite crystals has been discussed as another likely mechanism (Carlson and Christensen, 1979; Milholland et al., 1980; Schaftenaar and Carlson, 1984; O'Brien, 1990).

A dependency of acoustic anisotropy in marine sediments on the overall content of $CaCO_3$ has also been suspected, although no specific genetic origin is implied. O'Brien (1990) showed for some calcareous claystones of ODP Holes 603B and 672A a positive correlation of calcite content and acoustic anisotropy, while an inverse trend was found by Carlson et al. (1983) for pelagic chalks and limestones.

Compactional anisotropy—parallel alignment of pores and particles normal to bedding due to gravitational compaction under increasing overburden—is commonly assumed to be the most important single source for the downhole increase in acoustic anisotropy in fine-grained, clay-rich sediments (Hamilton, 1970; Kim et al., 1983, 1985; O'Brien, 1990).

The importance of microfabric control has long been acknowledged, but rarely quantitatively evaluated. Ramos and Rathmell (1989) demonstrated how the orientation of microfractures and microcracks controls the spatial configuration of acoustic anisotropy in sandstone core samples. By continuously mapping the direction of maximum acoustic anisotropy, they were able to verify the direction of maximum in-situ compressive stress, which was also independently determined through other methods.

In summary it can be said that acoustic anisotropy in marine sediments has been identified as a common phenomenon, the sources of which are—although theoretically reasonably well understood—rarely quantitatively determined or constrained through experimental work.

METHODS

Compressional-wave (P-wave) velocity measurements were obtained using two different systems on board *JOIDES Resolution* during Leg 131, depending on the degree of lithification of the sediment. P-wave velocities were measured in softer sediment using a Dalhousie University/Bedford Institute of Oceanography digital sound velocimeter (DSV). Velocity calculation is based on the accurate measurement of the delay time of an impulsive acoustic signal traveling between a pair of piezoelectric transducers inserted in the split sediment cores. The transducers that were used emit a 2-μs square wave at about 250 and 750 kHz. The transmitted and received signals were digitized by a Nicolet 320 digital oscilloscope and selection of first-arrival and velocity calculations were performed by a dedicated microcomputer. Two transducers were used, separated by approximately 7 cm, measuring the vertical (along the core axis) and transverse (normal to the core axis) P-wave velocity. Periodically, the separation was precisely evaluated by running a calibration procedure in distilled water. At each sampling interval (normally two per section), the transducers were carefully inserted into the split section and velocity measured in both directions.

The Hamilton frame velocimeter (Boyce, 1976) was used to measure compressional-wave velocities at 500 kHz in discrete sediment samples when induration made it difficult to insert the DSV transducers without making any perturbations around them and in lithified sediments and basement rocks when insertion became impossible. Samples were carefully cut using a double-bladed diamond saw. Sample thickness was measured directly from the velocimeter-frame lead screw through a linear resistor output to a digital multimeter. Zero travel times for the velocity transducers were estimated by linear regression of traveltime vs. distance for a series of aluminum and lucite standards. Filtered seawater was used to improve the acoustic contact between the sample and the transducers. The DSV oscilloscope and processing software were used to digitize waveforms, to calculate velocities, and to store the waveforms for later attenuation calculations.

An orientation procedure using paleomagnetic data is described in great detail for structural data in Table 6 in the "Explanatory Notes" section of Taira et al. (1991). Acoustic anisotropies were derived from P-wave measurements on physical property samples that were cut with a double-bladed saw from the working-half of the cores. As the transverse P-wave velocity was always measured in the direction normal to the surface of the working-half, it is possible to apply an equivalent orientation procedure.

SHIPBOARD RESULTS

General

Leg 131 was targeted at the Nankai Trough accretionary prism, which represents a type example for convergent margins characterized by a high input of clastic sediment. This class of accretionary margins is the most frequently occurring type among the circum-Pacific plate boundaries. The working area (Fig. 1A) is characterized by a regular tectonic style of imbricate thrusting and the shallow depth of the décollement zone in combination with a high regional heat flow, making it an ideal choice for the evaluation of questions pertaining to clastic prisms in general. Studies on the interdependency of deformational processes, physical properties, structural development, and hydrology in accreting and accreted sediment were among the prime goals of this cruise. Many of these objectives could be accomplished by drilling Site 808 in the frontal part of the toe of the accretionary wedge (Taira et al., this volume). Site 808 provided—for the first time in the history of ocean drilling—a continuous profile through the accretionary sequence, the décollement, and the subducting sequence into the top of the oceanic crust in the toe region of an accretionary wedge (Fig. 1B). One of the most striking features of Site 808 is the strong dichotomy in structural styles and downhole physical property trends above and below the décollement. Many deformational structures covering a wide range of scales were found between frontal thrust and décollement, reflecting the compressional tectonic regime in the frontal deformation zone of the prism. Below the décollement virtually no signs of deformation could be detected, indicating a complete mechanical decoupling between the accreting and the subducting portion of the sedimentary sequence.

Index Physical Properties

All mass physical properties display an irregular downhole profile with major discontinuities across the frontal thrust and the décollement. While offsets occurring across the frontal thrust can be explained by the stratigraphic repetition of ca. 160 m, a fundamentally different genetic origin has to be assumed for the décollement. Between frontal thrust and décollement porosity, bulk density and water content show steady—albeit lithologically modulated—downhole trends, compatible with a normally consolidated-to- slightly overconsolidated state of the accreting sediments. The narrow (20 m wide) décollement zone itself is characterized by brittlely deformed, hardened sediments of low porosity and high density. Below the décollement another strong offset to higher porosity and lower density sediment marks the top of the subducting sequence. It has been suggested that an impermeable or overpressured décollement restricts dewatering of this sequence, causing high excess pore pressures and underconsolidation. This model is in good agreement with porosity and density profiles within the subducting sediments. All physical properties are discussed in detail in (Taira et al., 1991).

Compressional-Wave (P-Wave) Velocity Data

Being largely a function of lithology (grain density) and packing structure of particles (porosity), the downhole development of compressional (P-wave) velocity at Site 808 closely matches the observed trends in sediment mass physical properties. Due to sampling problems in the coarse-grained turbiditic sediments above the frontal thrust, few reliable velocity data (V_{pl} and V_{pt}) could be determined in the accreted sequence above the frontal thrust (Fig. 2A, 2B). Within the interval between thrust and décollement (365–945 mbsf), longitudinal and transverse acoustic velocities are increasing in a complex cyclic pattern that is likely to be affected by ash content in hemipelagic sediments. In the sediments of the outer marginal trench wedge

(409–557 mbsf) and those belonging to the transitional zone (557-618 mbsf) and the upper Shikoku Basin sediments (618–829 mbsf), velocities are scattered over a broad band, that narrows considerably in the hemipelagic deposits of the Lower Shikoku Basin (824–1243 mbsf). While velocities in the décollement zone itself are widely scattered with no apparent downhole trend, an abrupt offset to lower velocities defines the onset of the subducting sedimentary sequence, followed by a regular increase in both V_{pl} and V_{pt}. This agrees well with the observed changes in other physical properties.

The large number of physical property data sets with both V_{pl} and V_{pt} available offers a unique opportunity to study the impact of the aforementioned parameters on acoustic anisotropy. The first review of all available data reveals no clear downhole pattern in acoustic anisotropy, the expected "normal" trend of increasing anisotropy with depth can not be found (Fig. 3). On the contrary, a gradual decrease between frontal thrust and décollement can be found that reverts below the décollement. Unlike other physical parameters, acoustic anisotropy does not define the décollement with a clear discontinuity, but rather covers the interval between frontal thrust and base of subducting sediments with a band of scatter approximately 20% wide.

ACOUSTIC ANISOTROPY

Evaluation of Possible Mechanisms

In the course of the following sections, the discussed possible causes of acoustic anisotropy are reviewed with respect to the Site 808 data. To constrain the following analysis to the appropriate lithologies, the first step necessary is a screening process of all lithological descriptions to exclude unusual or unrepresentative lithologies from further discussion. It is evident that the high degree of variability in acoustic anisotropy can be attributed to compositional changes: Units II (556.8–618.5 mbsf) and IVa (618.5–823.7 mbsf) are characterized by frequent ash and tuff layers, resulting in the highest degree of scatter observed in Hole 808C. Most authors cited in the previous sections have discussed acoustic anisotropy with respect to a specific lithology, mostly fine-grained, either clayey or calcareous pelagic to hemipelagic sediment, which is the "target" lithology for the following tests.

The screening of the available data excluded mostly coarse grained (from sandstone dikes) or monomineralic (pure ash) samples from the accreting section, which is characterized over large intervals by coarse-grained turbiditic trench sediment with low clay content. Physical property data sets from samples with $CaCO_3$ content higher than the average background level of 20% were also removed from further analysis. Based on these same criteria, only a few points had to be removed from the original data set below the décollement, where sediments are predominantly of hemipelagic origin (Fig. 4).

Graphical and statistical comparison of downhole profiles revealed no linear correlation of $CaCO_3$ content and acoustic anisotropy, that was demonstrated by O'Brien (1990) to exist in some calcareous claystones. The correlation coefficient found for this data set does not suggest a comparable interrelation ($r = 0.09$) (Fig. 5).

Measuring P-wave velocities on standard ODP physical property samples to calculate acoustic anisotropies has an inherent source of error. As physical property sample cubes are cut with faces perpendicular and parallel to the surface of the working core half and the core walls, all P-wave velocities are determined either parallel or normal to the core axis, which is therefore the reference frame for the calculated acoustic anisotropy. O'Brien et al. (1989) demonstrated a good correlation between bedding angle and acoustic anisotropy in hemipelagic mudstones from the Japan Trench with acoustic anisotropies decreasing from positive values at low degrees of bedding dip to negative values at high angles of bedding dip. As no measurements of bedding dip angles were made directly on physical property samples, the extensive structural data base was employed to compare the two parameters.

Taking all available data for samples of Unit IVb (lower Shikoku Basin sediment), which are of a similar hemipelagic lithology (Figs. 6A, 6B), no correlation of this type could be identified.

Several studies have suggested that primary acoustic anisotropy can be generated through depositional processes, e.g., sedimentation in a depositional regime dominated by currents (see Introduction). As the different lithological units encountered at Site 808 are defined under consideration of their depositional environment, we would expect different levels of correlation in different layers of the sequence. Judging from the very low correlation coefficients found for most units (Fig. 7), this is obviously not the case. Correlation of acoustic anisotropy with depth for different lithological units did not indicate a clear downhole trend in any of the Site 808 units except for Unit IVb, which displays decreasing acoustic anisotropy above and increasing acoustic anisotropy below the décollement (Fig. 7).

Because lithologic Unit IVb in Site 808 is actually dissected by the décollement, it is possible to directly evaluate the response to accretion vs. subduction for a defined sediment type. The Unit IVb, termed lower Shikoku Basin sediment, is composed of a fairly coherent hemipelagic lithology over a range of about 420 m. Therefore only this part of the section at Site 808 is considered for further analysis (Fig. 8). There is no clear correlation of anisotropy with downhole depth—on the contrary a slight decrease in the accreting part of the lower Shikoku Basin sediments vs. a clear increase in the subducting part of the sequence indicates that this property is related to the process of accretion and the resulting compressive forces.

REORIENTATION

To evaluate the possible correlation of acoustic anisotropy direction and the direction of maximum compressive strain, paleomagnetic data were employed; using an existing paleomagnetic data set from Hole 808C, all individual physical property samples on which acoustic data were obtained, were oriented to yield acoustic anisotropy as a function of geographical direction. This information was then used to compare accreted vs. subducted sediments in terms of their directional properties (as described in the "Methods" section).

To identify directional information of acoustic anisotropy a polar plot graph was prepared: it depicts a comparison of averaged acoustic anisotropies from the lower Shikoku Basin sediments above vs. below the décollement (Fig. 9). Acoustic anisotropy is averaged over 10° intervals taking a range of 0° to 180° as a basis. To simplify the visual interpretation, mirrored averages were also plotted in the respective 180° to 360° range. Although the total number of data sets used here is relatively small (86 data sets cover a range of 120 m above, 102 data sets cover a range of 278 m below the décollement), this plot shows a considerable difference between both data sets. While acoustic anisotropy in the accreting sediments shows peak values in the direction parallel to the subduction vector (315°) and perpendicular to that, no such preferential orientation can be found in the anisotropies below the décollement.

ERROR ANALYSIS

P-wave velocity measurements are inherently difficult, as first arrivals are difficult to determine (Birch, 1986). Great care must therefore be taken to evaluate and characterize sources and proportions of possible errors. Most earlier attempts to analyze acoustic anisotropies from DSDP and ODP P-wave velocity data did not include studies of error propagation, although the instrumental accuracy is in many cases on the order of the observed effects. This is especially true for data generated during DSDP cruises and to a lesser extent for ODP equipment-derived data.

Using a slightly more cautious approach we have calculated the largest absolute errors according to Taylor's law as well as the mean absolute errors according to Gauss's law which both apply to com-
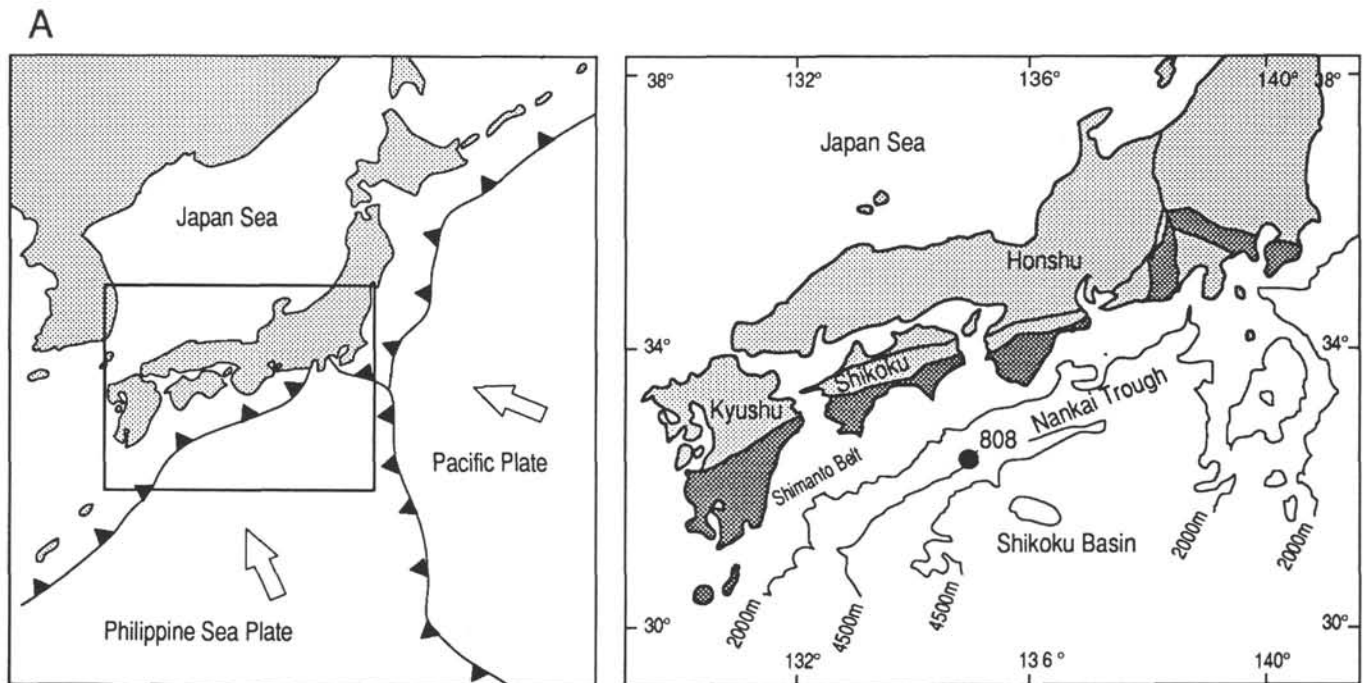
A

Figure 1. **A.** Plate boundaries and geotectonic reference frame around Japan, and location map of the Leg 131/Site 808 working area in the Nankai Trough accretionary complex (modified from Taira et al., 1991). **B.** Chronostratigraphy and lithofacies profile of Site 808 (original drawing provided by M. Underwood).

pound formulas that include several independent variables. This calculation was very well implemented for Unit IVb sediment, above the décollement only, as this data set is crucial to the validity of our conclusions. The largest errors are calculated assuming that all errors of individual variables in a compound formula add up in one direction, while the mean absolute errors are calculated considering the probabilistic chance that the effects of errors in individual variables are counterbalancing each other. Applying this concept to acoustic anisotropy, which is calculated according to:

$$A(1, t) = 200 \, (l-t) \, / \, (l + t),$$

where

A = acoustic anisotropy [%]
t = P-wave velocity normal to core axis (transverse)
l = P-wave velocity parallel to core axis (longitudinal),

we get as a mean absolute error (Gauss):

$$\Delta A = \sqrt{((\partial A / \partial 1) \Delta 1)^2 + ((\partial A / \partial t) \Delta t)^2}$$

and as the largest absolute error (Taylor):

$$\Delta A = |(\partial A / \partial 1) \Delta 1)^2 + |(\partial A / \partial t) \Delta t|.$$

Defining the partial derivatives (t/l):

$$\frac{\partial A}{\partial 1} = \frac{200 \, (1 + t) - 200 \, (1 - t)}{(1 + t)^2}$$

$$\frac{\partial A}{\partial l} = \frac{200 \, (1 = t) - 200 \, (l - t)}{(l + t)^2}$$
$$= \frac{400 \, t}{(l + t)^2}$$

and assuming a 1% precision (Boyce, 1976) for all P-wave velocity in a Hamilton frame velocimeter, Gauss and largest error are calculated as follows:

if $\Delta l = l$, then $1\% = 0.01 \, l$ and $\Delta \tau = t$, then $1\% = 0.01 \, t$ and the following holds:

Gauss error:

$$\Delta A = \sqrt{(400 \, t/(l + t)^2)^2 \, (0.01 \, l)^2 + (400 \, l/(l + t)^2 \, (0.01 \, t)^2}$$
$$= \sqrt{(4 \, l t / (l + t)^2)^2 + (4 \, l t / (l + t)^2)^2}$$
$$= \sqrt{2 \, (4 \, l t / (l + t)^2)^2}$$
$$= \sqrt{2 \, (4 \, l t / (l + t)^2)^2}$$

largest error:

$$\Delta A = (400 \, t/(l + t)^2) \, 0.01 \, l + (400 \, l/(l + t)^2) \, 0.01 \, t$$
$$= 4 \, l t / (l + t)^2 + 4 \, l t / (l + t)^2$$
$$= 8 \, l t / (l + t)^2$$

Errors calculated according to this procedure are given in Table 1. It turns out that maximum and mean absolute errors are on the order of the observed effects in a number of instances. However, all P-wave measurements made on board were normally repeated twice or more times if necessary to assure a high degree of reproducibility. The actual error is therefore likely to be much smaller in all data sets, which seem critical according to our study. Nevertheless, it is obvious that much more attention should be given to possible errors in comparative analysis of acoustic anisotropies. A critical review of laboratory procedures as well as of data treatment and the application of error propagation theory to studies of this type seems to be critical, especially when only a small number of data sets is used.
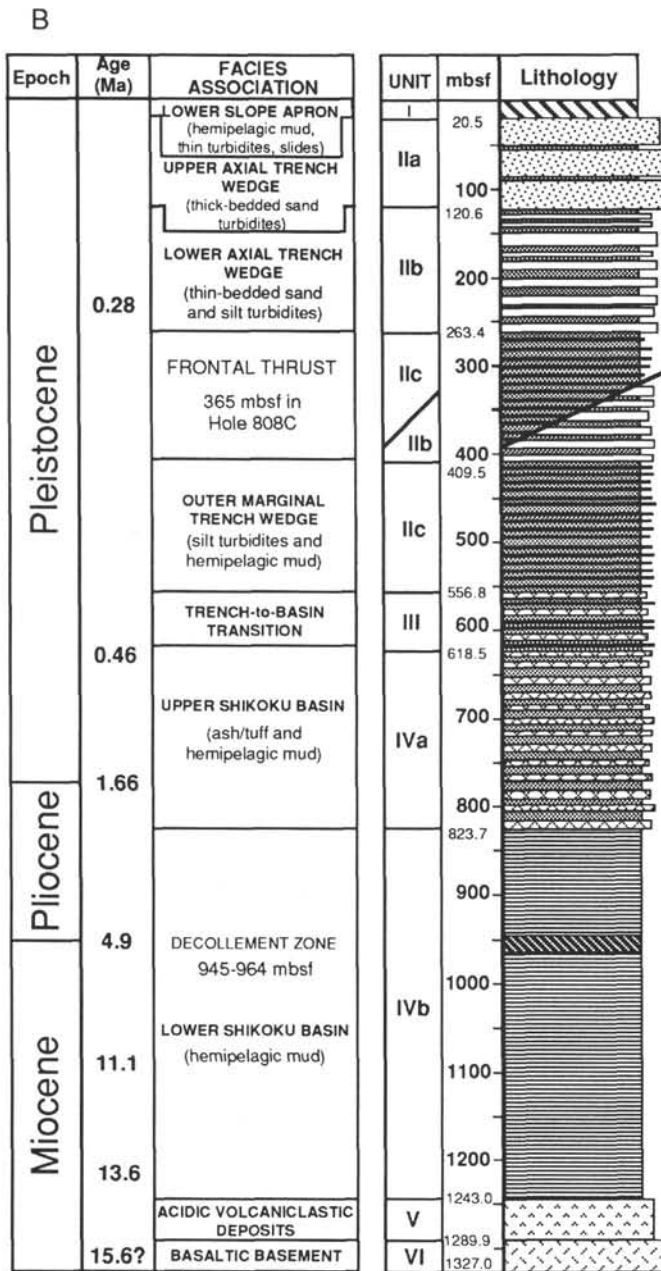
B

Epoch	Age (Ma)	FACIES ASSOCIATION	UNIT	mbsf	Lithology
Pleistocene	0.28	LOWER SLOPE APRON (hemipelagic mud, thin turbidites, slides)	I	20.5	
		UPPER AXIAL TRENCH WEDGE (thick-bedded sand turbidites)	IIa	100 120.6	
		LOWER AXIAL TRENCH WEDGE (thin-bedded sand and silt turbidites)	IIb	200 263.4	
		FRONTAL THRUST 365 mbsf in Hole 808C	IIc / IIb	300 400 409.5	
	0.46	OUTER MARGINAL TRENCH WEDGE (silt turbidites and hemipelagic mud)	IIc	500 556.8	
		TRENCH-to-BASIN TRANSITION	III	600 618.5	
Pliocene	1.66	UPPER SHIKOKU BASIN (ash/tuff and hemipelagic mud)	IVa	700 800 823.7	
	4.9	DECOLLEMENT ZONE 945-964 mbsf	IVb	900 1000	
Miocene	11.1 13.6	LOWER SHIKOKU BASIN (hemipelagic mud)		1100 1200 1243.0	
	15.6?	ACIDIC VOLCANICLASTIC DEPOSITS	V	1289.9	
		BASALTIC BASEMENT	VI	1327.0	

Figure 1 (continued).

must, therefore, consider structurally controlled acoustic anisotropy as one option.

It is well established in the literature about the correlation of P- and S-wave velocities and microfabrics, that not only grain fabric but also microcracks and microfractures can have an important impact on the development of acoustic anisotropy.

Preferential orientation of acoustic anisotropies has been used to determine fracture direction in areas of pervasive microfracturing to identify the orientation of the maximum in-situ stress (Ramos and Rathmell, 1989; Yale and Sprunt, 1989). Microcrack orientation can be directly inferred from the direction of maximum and minimum acoustic anisotropies, as microcracks or microfractures impede and deflect the propagation of sonic energy, yielding highest P-wave velocities along strike and lowest perpendicular to strike.

The generation of these structures is discussed in detail by Ramos and Rathmell (1989). If these discontinuities are relaxation features that formed as stress-relief microcracks, their strike will be perpendicular to the direction of maximum horizontal in-situ stress (S_{hmax}), while tensile microcracks that may form as precursors to coring-induced tensile macrofractures will be parallel to S_{hmax}. With the reoriented anisotropies at hand it is possible to speculate about the character of microfractures leading to the observed correlation of convergence direction and acoustic anisotropy.

If microfractures are formed at Site 808 cores as *stress relief features* perpendicular to the direction of the maximum horizontal in-situ stress (given through the direction of convergence), then V_{pt} must be slowest in the direction of 315°. As a corollary, highest acoustic anisotropies should be found in that direction. Microfractures forming in Site 808 cores as *tensile fractures* parallel to the maximum horizontal in-situ stress should result in highest P-wave velocities normal to the convergence vector, yielding smallest acoustic anisotropies parallel to 315°. Because maximum values in acoustic anisotropy are found in both of these directions, it is possible that both mechanisms contribute to the observed pattern. High-resolution electron microscopy might be able to reveal the true configuration of microfractures to support this preliminary interpretation.

It has been argued that grain fabric in the sequence between frontal thrust and décollement was strongly affected by the process of off-scraping and accretion, resulting in unusual acoustic properties. Judging from the data and results presented here, it is not necessary to invoke such a mechanism to describe the acoustic anisotropies found.

This conclusion is also in good agreement with data from X-ray goniometry studies, which suggest that grain fabric was not significantly altered by lateral compression in the wedge toe (Behrmann and Kopf, this volume).

The normal expected trend of acoustic anisotropy observed below the décollement reflects, on the other hand, an inherited property from basinal processes, where normal gravitational compaction and accompanying grain rearrangement are the predominant controlling factors for acoustic properties.

DISCUSSION

As is obvious from our review of possible causes of acoustic anisotropy, the commonly assumed depositional, diagenetic, or compactional processes cannot be invoked to explain the observed trends at Site 808. Oriented clay minerals, which are highly anisotropic in themselves, do not contribute to the observed pattern in acoustic anisotropy because they maintain a rather uniform background concentration of 12%–22% throughout the complete section in Site 808.

On the other hand, it is clear from the results of the reorientation procedure we have utilized here, that acoustic anisotropy is somehow linked to the stress regime in the toe region of the Nankai Trough accretionary complex. The accreting sedimentary sequence between frontal thrust and décollement in Site 808 abounds with convergence-related deformational features covering a wide range of scales. We

SUMMARY

Using the extensive shipboard physical property data set from Site 808 we have evaluated possible causes of the irregular downhole development of acoustic anisotropies in accreted sediment of the Nankai Trough accretionary prism. After various steps of data reduction and screening and testing of various hypotheses proposed by previous workers to describe the generation of acoustic anisotropy, we were not able to identify among them a single source or a likely mechanism to explain the observed trends. A paleomagnetic reorientation procedure was applied to all physical property data sets to yield true geographic bearing of acoustic anisotropies. The results facilitated the integration of the observed changes in physical properties with the geotectonic framework at the deformation front of the Nankai Trough accretionary complex.
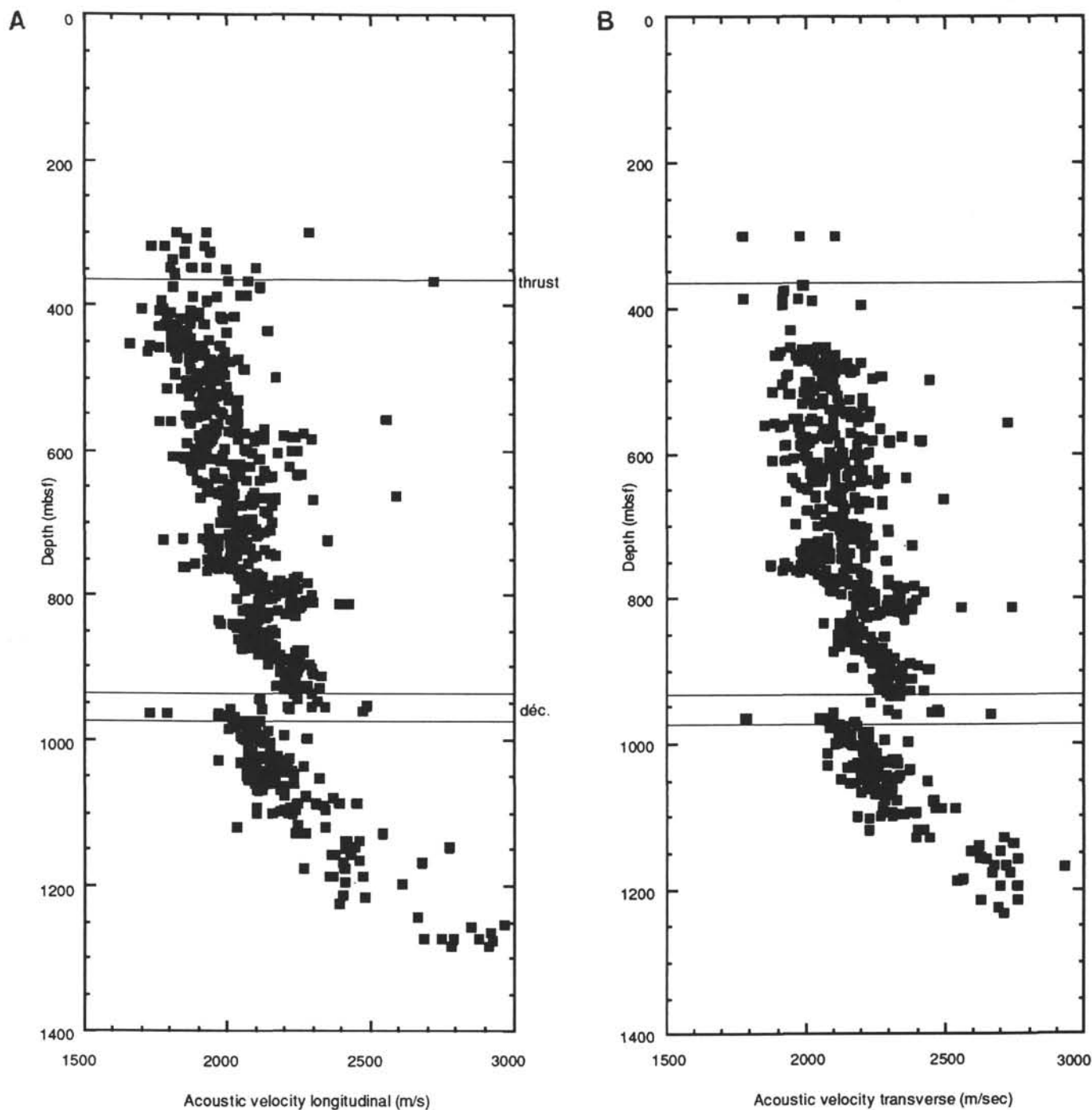
Figure 2. **A.** Acoustic velocity longitudinal (parallel to core axis) vs. depth at Site 808. **B.** Acoustic velocity transverse (normal to core axis) vs. depth at Site 808.

While accreted sediment between frontal thrust and décollement shows strongest acoustic anisotropies in the direction parallel and normal to the direction of subduction, no obvious directional preference of this property can be found in lithologically equivalent sediment below the décollement. This result supports the conclusion that the compressive tectonic regime in the frontal part of the Nankai Trough accretionary wedge alters directional acoustic properties in a predictable manner. Formation of tensile as well as stress relief microfractures parallel and perpendicular to the convergence-related compressional stress defines the observed orientation of maximum acoustic anisotropy. In the absence of this compressional stress no

such control is active below the décollement, where an inherited basinal anisotropy pattern prevails. To verify the model proposed here, further SEM studies and oriented in-situ measurements of acoustic properties are necessary.

ACKNOWLEDGMENTS

was financially supported by the Deutsche Forschungsgemeinschaft (DFG). R. Benett and N. I. Christensen reviewed the manuscript and provided helpful suggestions.

REFERENCES

Birch, F., 1986. The velocity of compressional waves in rocks to 10 kilobars, part 1. *J. Geophys. Res.*, 1083–1102.

Boyce, R.E., 1976. Definitions and laboratory techniques of compressional sound velocity parameters and wet-water content, wet-bulk density, and porosity parameters by gravimetric and gamma ray attenuation techniques. *In* Jackson, E.D., Schlanger, S.O., et al., *Init. Repts. DSDP*, 33: Washington (U.S. Govt. Printing Office), 931–958.

Carlson, R.L., and Christensen, N.I., 1977. Velocity anisotropy and physical properties of deep sea sediments from the Western South Atlantic. *In* Perch-Nielsen, K., Supko, P.R., et al., *Init. Repts. DSDP*, 39: Washington (U.S. Govt. Printing Office), 555–559.

————, 1979. Velocity anisotropy in semi-indurated deep sea sediments. *J. Geophys. Res.*, 84:205–211.

Carlson, R.L., Schaftenar, C.H., and Moore, R.P., 1983. Causes of compressional wave anisotropy in calcareous sediments from the Rio Grande Rise. *In* Barker, P.F., Carlson, R.L., and Johnson, D.A., et al., *Init. Repts. DSDP*, 72: Washington (U.S. Govt. Printing Office), 565–576.

Bachman, R.T., 1979. Acoustic anisotropy in marine sediments and sedimentary rocks. *J. Geophys. Res.*, 84:7661–7663.

Fuji, N., 1981. Anisotropy in compressional wave velocity and wet-bulk densities of calcareous sedimentary rocks, Deep Sea Drilling Project Leg 62. *In* Thiede, J., Vallier, T.L., et al., *Init. Repts. DSDP*, 62: Washington (U.S. Govt. Printing Office), 995–998.

Hamilton, E.L., 1970. Sound velocity and related properties of marine sediments, North Pacific. *J. Geophys. Res.*, 75:4423–4446.

Kim, D.-C., Katahara, K.W., Manghnani, M.H., and Schlanger, S.O., 1983. Velocity and attenuation in deep-sea carbonate sediments. *J. Geophys. Res.*, 88:2337–2343.

Kim, D.-C., Manghnani, M.H., and Schlanger, S.O., 1985. The role of diagenesis in the development of physical properties of deep-sea carbonate sediments. *Mar. Geol.*, 69:69–91.

Milholland, P., Manghnani, M.H., Schlanger, S.O., and Sutton, G., 1980. Geoacoustic modeling of deep-sea carbonate sediments. *J. Acoust. Soc. Am.*, 68:1351–1360.

Nacci, V.A., Wang, M.C., and Gallagher, J., 1974. Influence of anisotropy and soil structure on elastic properties of sediments. *In* Hampton, L. (Ed.), *Physics of Sound in Marine Sediments:* New York (Plenum), 63–88.

O'Brien, D.K., 1990. Physical, acoustic, and electrical properties of deep-sea sediments [Ph.D. dissert.]. Univ. of Hawaii.

O'Brien, D.K., Manghnani, M.H. and Schoonmaker-Tribble, J., 1989. Irregular trends of physical properties in homogeneous clay-rich sediments of DSDP Leg 87 Hole 584, midslope terrace in the Japan Trench. *Mar. Geol.*, 87:183–194.

O'Brien, N.R., Nakazawa, K., and Tokuhashi, S., 1980. Use of clay fabric to distinguish turbiditic and hemipelagic siltstones and silt. *Sedimentology*, 27:47–61.

Postma, G.W., 1955. Wave propagation in a stratified medium. *Geophysics*, 20:780–806.

Ramos, G.G., and Rathmell, J.J., 1989. Effects of mechanical anisotropy on core strain measurements for in-situ stress determination. *In* Tomich, J.F.O. (Ed.), *Formation Evaluation and Reservoir Geology*. Exxon Prod. Res., Houston, and Soc. Pet. Eng. AIME, 64:1989.

Schaftenaar, C.H., and Carlson, R.L., 1984. Calcite fabric and acoustic anisotropy in deep-sea carbonates. *J. Geophys. Res.*, 89:503–510.

Taira, A., Hill, I., Firth, J.V., et al., 1991. *Proc. ODP, Init. Repts.*, 131: College Station, TX (Ocean Drilling Program).

Wetzel, A., 1986. Anisotropy and modes of deposition of pelitic Mississippi Fan deposits. *In* Bouma, A.H., Coleman, J.M., Meyer, A.W., et al., *Init. Repts. DSDP*, 96: Washington (U.S. Govt. Printing Office), 811–817.

Wetzel, A., 1987. Sedimentological significance of strain and sonic velocity anisotropy in fine-grained turbiditic and hemipelagic deep-sea sediments—an example from the Mississippi Fan. *Mar. Geol.*, 74:191–207.

Yale, D.P., and Sprunt, E.S., 1989. Prediction of fracture direction using shear acoustic anisotropy. *Log Analyst*, 30:65–70.
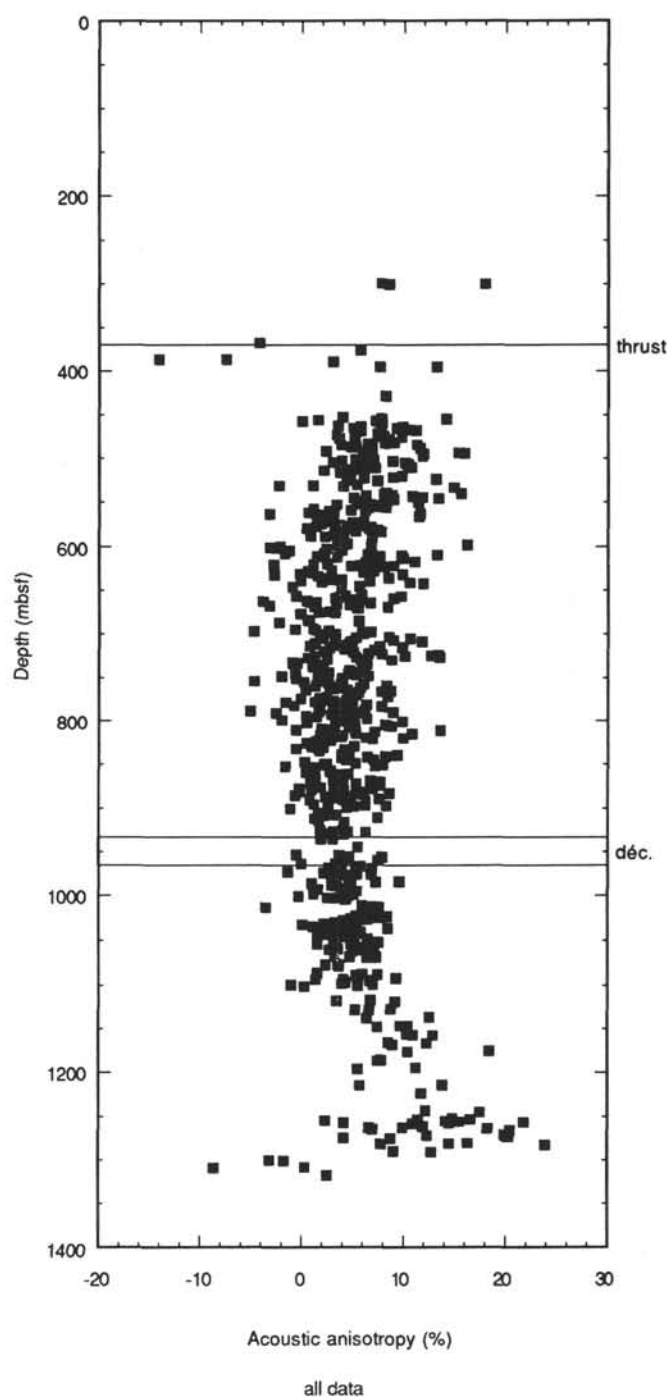
Figure 3. Acoustic anisotropy vs. depth at Site 808 using all available data.
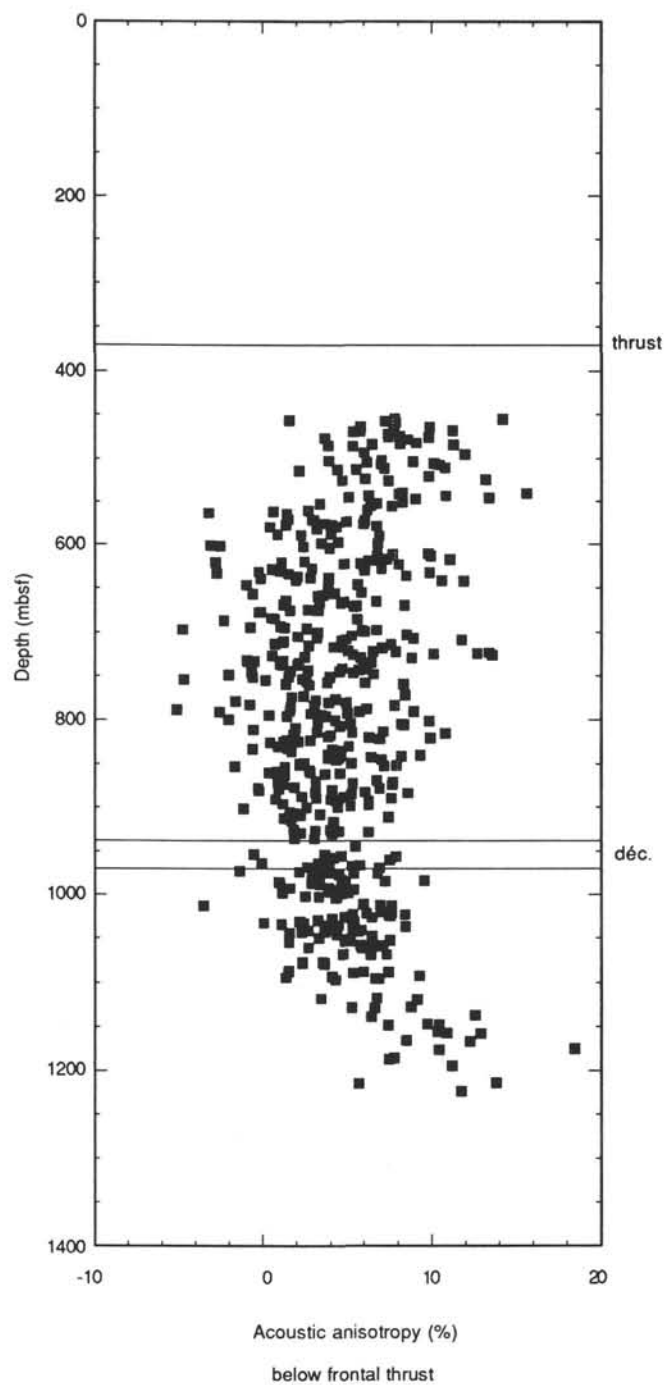
Figure 4. Acoustic anisotropy vs. depth at Site 808 below the frontal thrust.
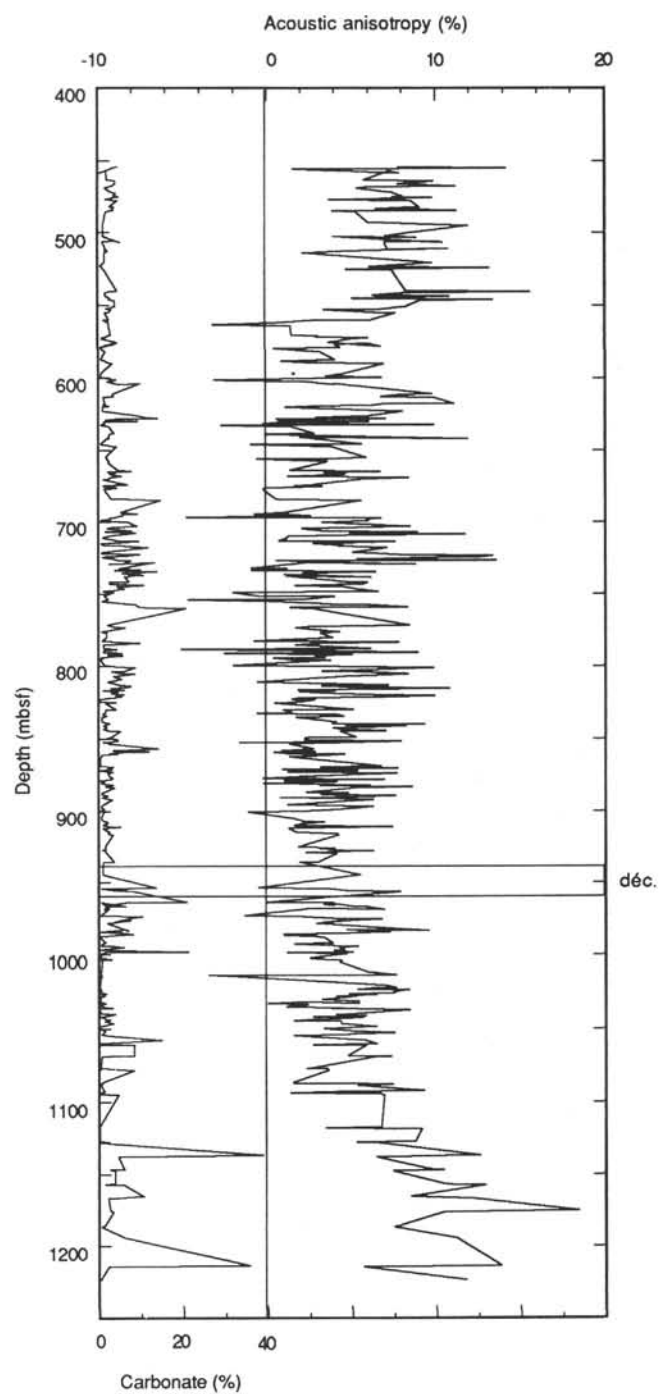
Figure 5. Comparison of CaCO$_3$ content and acoustic anisotropy vs. depth at Site 808.
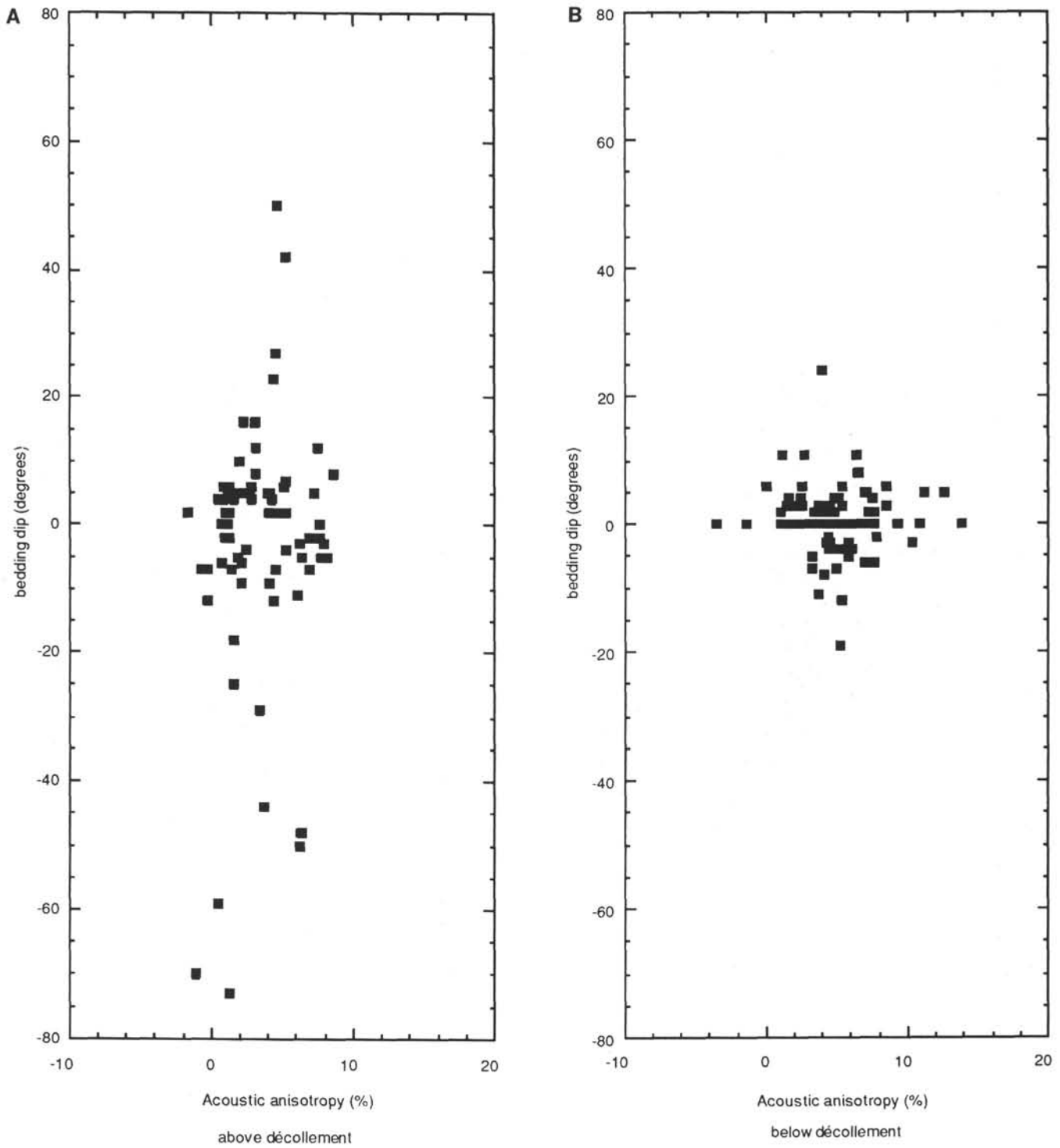
Figure 6. Acoustic anisotropy vs. bedding angle in the lower Shikoku Basin sediment at Site 808. **A.** Above décollement. **B.** Below décollement.
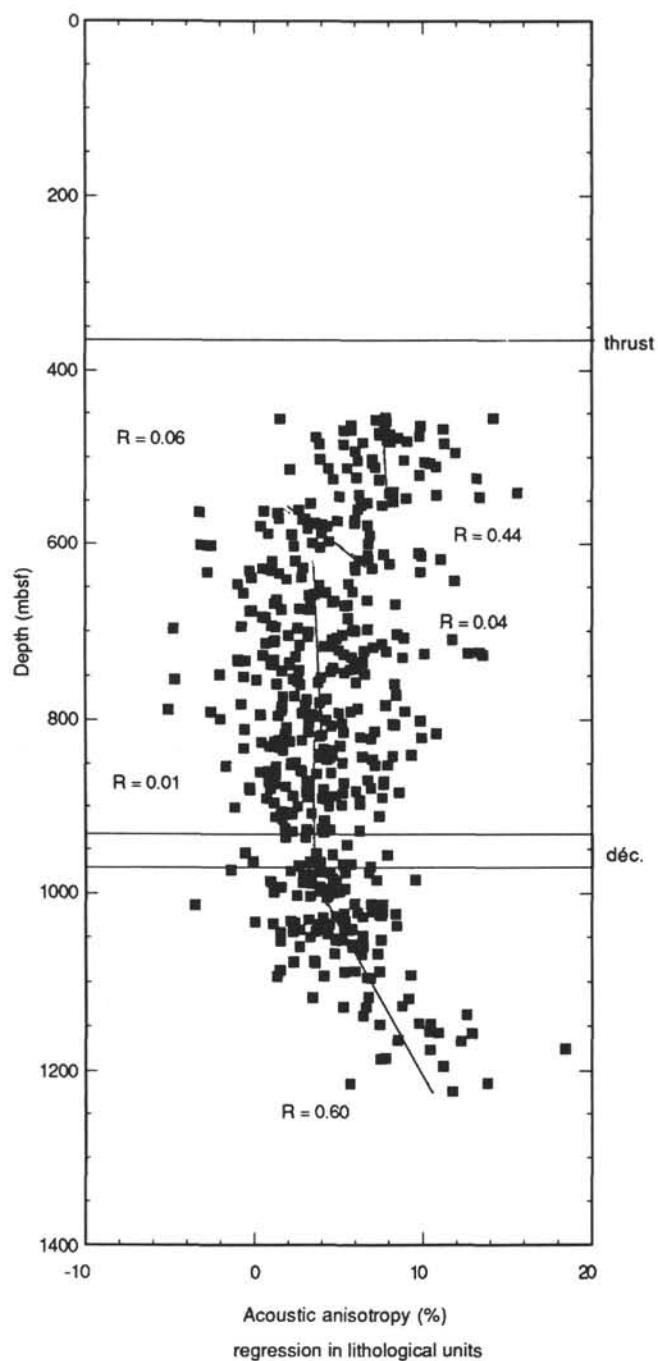
Figure 7. Regression of acoustic anisotropy vs. depth for different lithologic units at Site 808.

Figure 8. Regression of acoustic anisotropy vs. depth above and below the décollement at Site 808.

Figure 9. Composite graph of acoustic anisotropy in Unit IVb (lower Shikoku Basin sediments at Site 808) above (823–945 mbsf) and below (965–1243 mbsf) the décollement, orientation 0°–180°. Data are averaged over 10° intervals; arrow indicates direction of plate convergence (315°).

Table 1. Error analysis definitions for Unit IVb sediments above décollement in Hole 808C.

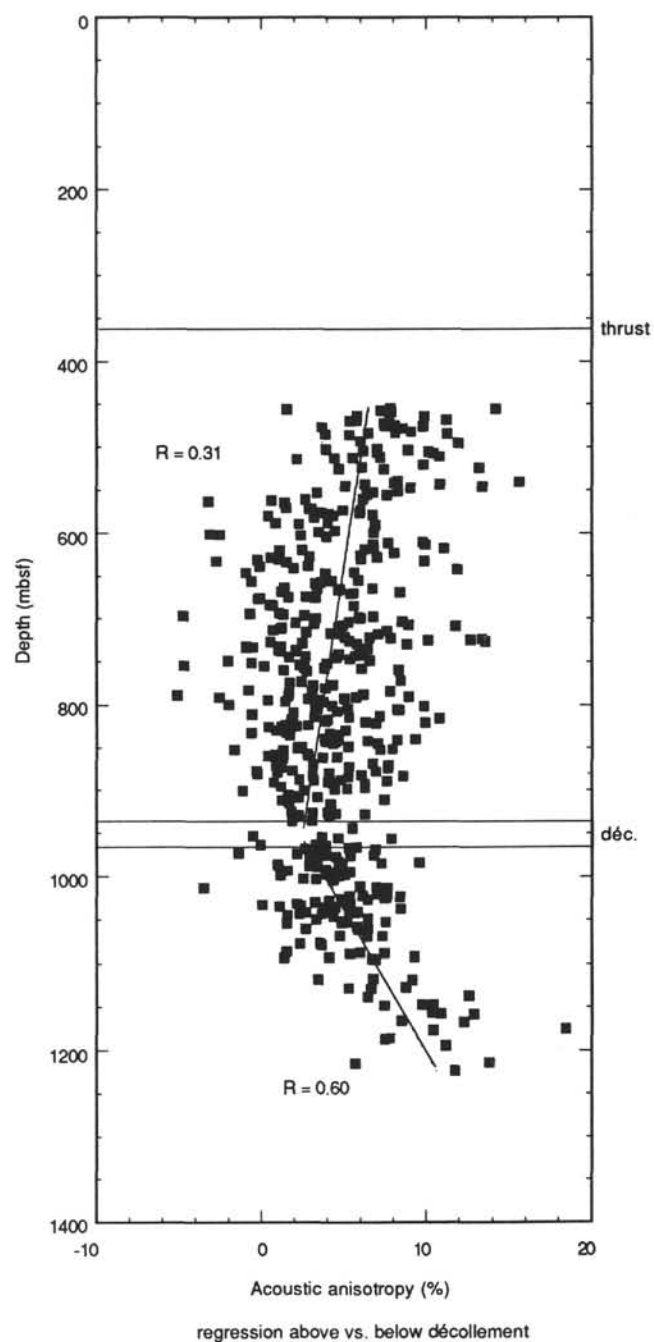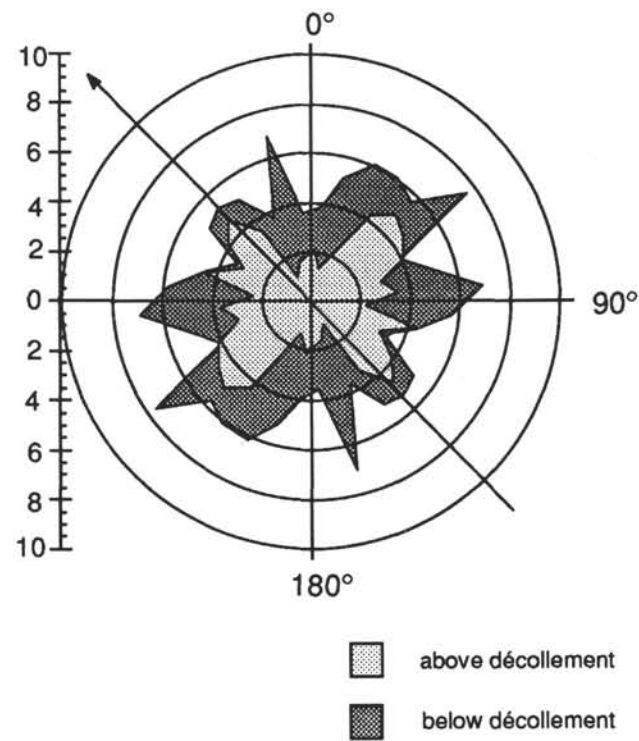| Core, section	Depth (mbsf)	Trans. vel. (%)	Long. vel. (%)	Acoustic aniso.	Taylor error	Rel. Taylor error	Aniso. - Taylor err.	Aniso. + Taylor err.	Gauss err. abs	Gauss err. rel.	Aniso. - Gauss err.	Aniso. + Gauss err.
131-808C-55R-4	823.4	2105	2165	2.81	1.99	71.15	0.81	4.81	1.41	0.5	1.4	4.22
55 4	824.4	2122	2167	2.1	1.99	95.3	0.1	4.1	1.41	0.67	0.68	3.51
55 5	825	2141	2167	1.21	1.99	165.68	-0.79	3.21	1.41	1.17	-0.21	2.62
55 5	825.6	2208	2217	0.41	1.99	491.66	-1.59	2.41	1.41	3.48	-1.01	1.82
56 1	829	2135	2164	1.35	1.99	148.23	-0.65	3.35	1.41	1.05	-0.06	2.76
56 1	829.7	2239	2355	5.05	1.99	39.58	3.05	7.05	1.41	0.28	3.64	6.46
56 2	830	2145	2165	0.93	1.99	215.5	-1.07	2.93	1.41	1.52	-0.49	2.34
56 2	831	2127	2172	2.09	1.99	95.52	0.09	4.09	1.41	0.68	0.68	3.51
56 3	832	2125	2157	1.49	1.99	133.81	-0.51	3.49	1.41	0.95	0.08	2.91
56 3	832.6	2138	2125	-0.61	1.99	327.92	-2.61	1.39	1.41	2.32	-2.02	0.8
56 4	833.4	2083	2171	4.14	1.99	48.32	2.14	6.14	1.41	0.34	2.72	5.55
56 5	834.5	1973	2064	4.51	1.99	44.34	2.51	6.51	1.41	0.31	3.09	5.92
56 5	835.3	2108	2144	1.69	1.99	118.1	-0.31	3.69	1.41	0.84	0.28	3.11
57 1	838.4	2102	2190	4.1	1.99	48.75	2.1	6.1	1.41	0.34	2.69	5.51
57 1	839.4	2068	2149	3.84	1.99	52.04	1.84	5.84	1.41	0.37	2.43	5.26
57 2	840	1976	2169	9.31	1.99	21.43	7.32	11.31	1.41	0.15	7.9	10.72
57 2	840.7	2035	2132	4.66	1.99	42.94	2.66	6.65	1.41	0.3	3.24	6.07
57 3	841.2	2022	2195	8.2	1.99	24.33	6.21	10.2	1.41	0.17	6.79	9.62
57 3	842.2	2057	2193	6.4	1.99	31.21	4.4	8.4	1.41	0.22	4.99	7.81
57 4	843.4	2079	2174	4.47	1.99	44.75	2.47	6.47	1.41	0.32	3.05	5.88
57 5	844.7	2057	2206	6.99	1.99	28.58	4.99	8.99	1.41	0.2	5.58	8.4
58 1	847.8	2159	2164	0.23	1.99	864.6	-1.77	2.23	1.41	6.11	-1.18	1.65
58 1	848.9	2091	2203	5.22	1.99	38.31	3.22	7.22	1.41	0.27	3.8	6.63
58 2	849.2	2064	2114	2.39	1.99	83.55	0.39	4.39	1.41	0.59	0.98	3.81
58 2	849.6	2120	2167	2.19	1.99	91.2	0.19	4.19	1.41	0.64	0.78	3.61
58 3	850.9	2077	2123	2.19	1.99	91.29	0.19	4.19	1.41	0.65	0.78	3.6
58 3	851.5	2106	2280	7.93	1.99	25.17	5.94	9.93	1.41	0.18	6.52	9.35
58 4	852.2	2082	2237	7.18	1.99	27.83	5.18	9.18	1.41	0.2	5.77	8.59
58 4	852.9	2174	2138	-1.67	1.99	119.77	-3.67	0.33	1.41	0.85	-3.08	-0.26
58 5	853.5	2089	2117	1.33	1.99	150.21	-0.67	3.33	1.41	1.06	-0.08	2.75
59 1	857.4	2128	2188	2.78	1.99	71.92	0.78	4.78	1.41	0.51	1.37	4.19
59 1	858.5	2117	2134	0.8	1.99	250.06	-1.2	2.8	1.41	1.77	-0.61	2.21
59 2	859.2	2072	2131	2.81	1.99	71.22	0.81	4.81	1.41	0.5	1.39	4.22
59 2	859.7	2137	2146	0.42	1.99	475.88	-1.58	2.42	1.41	3.36	-0.99	1.83
59 3	860.2	2136	2159	1.07	1.99	186.74	-0.93	3.07	1.41	1.32	-0.34	2.49
59 3	860.8	2140	2241	4.61	1.99	43.35	2.61	6.61	1.41	0.31	3.2	6.02
59 4	861.7	2039	2116	3.71	1.99	53.94	1.71	5.71	1.41	0.38	2.29	5.12
59 4	862.6	2085	2112	1.29	1.99	155.44	-0.71	3.29	1.41	1.1	-0.13	2.7
60 1	866.9	2095	2124	1.37	1.99	145.48	-0.63	3.37	1.41	1.03	-0.04	2.79
60 2	869	2129	2278	6.76	1.99	29.54	4.76	8.76	1.41	0.21	5.35	8.17
60 2	869.8	2154	2223	3.15	1.99	63.42	1.15	5.15	1.41	0.45	1.74	4.57
60 3	870.5	2084	2251	7.7	1.99	25.92	5.71	9.7	1.41	0.18	6.29	9.12
60 3	871	2158	2177	0.88	1.99	228.15	-1.12	2.88	1.41	1.61	-0.54	2.29
60 4	871.4	2174	2263	4.01	1.99	49.83	2.01	6.01	1.41	0.35	2.6	5.43
60 4	872.1	2092	2206	5.3	1.99	37.68	3.31	7.3	1.41	0.27	3.89	6.72
60 5	873.3	2077	2103	1.24	1.99	160.77	-0.76	3.24	1.41	1.14	-0.17	2.66

Table 1 (continued).

Core, section			Depth (mbsf)	Trans. vel. (%)	Long. vel. (%)	Acoustic aniso.	Taylor error	Rel. Taylor error	Aniso. - Taylor err.	Aniso. + Taylor err.	Gauss err. abs	Gauss err. rel.	Aniso. - Gauss err.	Aniso. + Gauss err.
131-808C-60R-5			874	2051	2215	7.69	1.99	25.97	5.69	9.69	1.41	0.18	6.28	9.1
	61	1	876.6	2249	2292	1.89	1.99	105.59	-0.11	3.89	1.41	0.75	0.48	3.31
	61	1	877.7	2265	2258	-0.31	1.99	646.14	-2.31	1.69	1.41	4.57	-1.72	1.1
	61	2	878.2	2117	2269	6.93	1.99	28.82	4.93	8.93	1.41	0.2	5.52	8.34
	61	2	879	2270	2292	0.96	1.99	207.36	-1.04	2.96	1.41	1.47	-0.45	2.38
	61	3	879.8	2152	2243	4.14	1.99	48.28	2.14	6.14	1.41	0.34	2.73	5.55
	61	4	881.2	2242	2237	-0.22	1.99	895.82	-2.22	1.78	1.41	6.33	-1.64	1.19
	61	4	882.3	2182	2318	6.04	1.99	33.06	4.05	8.04	1.41	0.23	4.63	7.46
	61	5	882.8	2160	2229	3.14	1.99	63.59	1.14	5.14	1.41	0.45	1.73	4.56
	61	5	883.5	2112	2302	8.61	1.99	23.19	6.61	10.61	1.41	0.16	7.2	10.02
	61	6	884.4	2144	2260	5.27	1.99	37.94	3.27	7.27	1.41	0.27	3.85	6.68
	62	3	889.6	2203	2377	7.6	1.99	26.28	5.6	9.6	1.41	0.19	6.19	9.01
	62	3	890.6	2201	2292	4.05	1.99	49.35	2.05	6.05	1.41	0.35	2.64	5.46
	62	4	890.8	2221	2238	0.76	1.99	262.29	-1.24	2.76	1.41	1.85	-0.65	2.18
	62	4	891.7	2250	2348	4.26	1.99	46.9	2.26	6.26	1.41	0.33	2.85	5.68
	62	5	892.4	2255	2401	6.27	1.99	31.86	4.27	8.27	1.41	0.23	4.86	7.68
	63	1	895.9	2142	2168	1.21	1.99	165.76	-0.79	3.21	1.41	1.17	-0.21	2.62
	63	1	897	2290	2439	6.3	1.99	31.71	4.3	8.3	1.41	0.22	4.89	7.71
	63	2	898.3	2225	2344	5.21	1.99	38.37	3.21	7.21	1.41	0.27	3.8	6.62
	63	3	899.3	2187	2286	4.43	1.99	45.16	2.43	6.43	1.41	0.32	3.01	5.84
	63	4	901.1	2297	2271	-1.14	1.99	175.68	-3.14	0.86	1.41	1.24	-2.55	0.28
	64	1	905.5	2296	2333	1.6	1.99	125.1	-0.4	3.6	1.41	0.88	0.18	3.01
	64	2	907.3	2221	2267	2.05	1.99	97.56	0.05	4.05	1.41	0.69	0.64	3.46
	64	2	908	2185	2260	3.37	1.99	59.25	1.38	5.37	1.41	0.42	1.96	4.79
	64	3	908.9	2232	2283	2.26	1.99	88.52	0.26	4.26	1.41	0.63	0.85	3.67
	64	3	909.8	2299	2337	1.64	1.99	122	-0.36	3.64	1.41	0.86	0.23	3.05
	64	4	910.2	2205	2240	1.57	1.99	126.99	-0.43	3.57	1.41	0.9	0.16	2.99
	64	4	911.1	2213	2384	7.44	1.99	26.85	5.44	9.44	1.41	0.19	6.03	8.85
	64	5	912.2	2326	2355	1.24	1.99	161.4	-0.76	3.24	1.41	1.14	-0.18	2.65
	65	1	915.2	2217	2254	1.66	1.99	120.83	-0.34	3.65	1.41	0.85	0.24	3.07
	65	2	917	2242	2338	4.19	1.99	47.69	2.19	6.19	1.41	0.34	2.78	5.61
	66	1	925.1	2277	2319	1.83	1.99	109.42	-0.17	3.83	1.41	0.77	0.41	3.24
	66	1	926	2172	2261	4.02	1.99	49.79	2.02	6.01	1.41	0.35	2.6	5.43
	66	2	926.4	2279	2350	3.07	1.99	65.18	1.07	5.07	1.41	0.46	1.65	4.48
	66	2	927.4	2320	2427	4.51	1.99	44.34	2.51	6.51	1.41	0.31	3.09	5.92
	66	3	928	2234	2378	6.24	1.99	32	4.25	8.24	1.41	0.23	4.83	7.66
	66	3	929	2262	2313	2.23	1.99	89.7	0.23	4.23	1.41	0.63	0.82	3.64
	66	4	930	2196	2288	4.1	1.99	48.72	2.1	6.1	1.41	0.34	2.69	5.52
	67	1	936	2235	2305	3.08	1.99	64.84	1.08	5.08	1.41	0.46	1.67	4.5

Note: Site, Core, Sect.: standard ODP core description; trans. vel.: P-wave velocity perpendicular to core axis; long. vel.: P-wave velocity parallel to core axis; acoustic aniso.: acoustic anisotropy; Taylor error: Taylor error (see text for discussion); rel. Taylor error.: Taylor error/acoustic anisotropy; aniso. – Taylor err.: acoustic anisotropy–Taylor error; aniso. + Taylor err. : acoustic anisotropy + Taylor error; Gauss error: Gauss error (see text for discussion); rel. Gauss error.: Gauss error/acoustic anisotropy; aniso. – Gauss err.: acoustic anisotropy–Gauss error; aniso. + Gauss err.: acoustic anisotropy + Gauss error.